# Single-Shot Receive-Only Ultrafast Electro-Optical Deflection Imaging

Chengshuai Yang,[1] Dalong Qi,[1] Fengyan Cao,[1] Yilin He,[1] Jiali Yao,[1] Pengpeng Ding,[1] Xiaoping Ouyang,[4] Yanzhong Yu,[5] Tianqing Jia,[1] Shixiang Xu,[2,†] Zhenrong Sun,[1,‡] and Shian Zhang[1,3,*]

[1] *State Key Laboratory of Precision Spectroscopy, School of Physics and Electronic Science, East China Normal University, Shanghai 200062, China*

[2] *Institute of Photonic Engineering, College of Electron Science and Technology, Shenzhen University, Shenzhen 518060, China*

[3] *Collaborative Innovation Center of Extreme Optics, Shanxi University, Taiyuan 030006, China*

[4] *Joint Laboratory on High Power Laser and Physics, Shanghai Institute of Optics and Fine Mechanics, Chinese Academy of Science, Shanghai 201800, China*

[5] *College of Physics and Information Engineering, Quanzhou Normal University, Quanzhou 362000, China*

(Received 12 December 2018; revised manuscript received 1 January 2020; accepted 17 January 2020; published 3 February 2020)

Imaging ultrafast dynamic events is a long-standing scientific goal. It is difficult for conventional electronic imaging sensors based on charge-coupled devices (CCDs) or complementary metal oxide semiconductors (CMOS) to capture dynamic processes occurring on the nanosecond or even shorter timescales due to the limitations of on-chip storage and electronic read-out speed. Here, we develop a dynamic imaging technique with a very simple compact configuration, called ultrafast electro-optical deflection imaging (UEODI), which has a temporal resolution of up to 20 ps or an imaging speed of $5 \times 10^{10}$ frames per second (fps), and therefore, it enables the observation of nanosecond and even picosecond dynamic events. UEODI operates in a single-shot receive-only mode, and thus, it is highly beneficial for imaging nonrepetitive (or irreversible) dynamic events and a variety of luminescent objects. Moreover, when combined with the time-of-flight (TOF) method, UEODI can detect three-dimensional (3D) objects. Using UEODI, we visualize a molecular photoluminescent process and measure a 3D ladder structure. Considering the capabilities of UEODI, it will have very importation application prospects in both basic research and applied science, including biomedical imaging.

DOI: 10.1103/PhysRevApplied.13.024001

## I. INTRODUCTION

High-speed imaging technology plays an indispensable role in solving countless scientific problems, advancing medicine, producing wonderful art, and revealing the inner workings of systems such as cells and even machines. The first practical application of high-speed imaging technology was the study by Muybridge in 1878 of whether all of the horse's feet leave the ground during galloping [1]. Recorded pictures of a supersonic bullet by Mach and Salcher in 1887 was another famous high-speed imaging experiment in that time period [2]. Since then, fascination with high-speed imaging has been increasing. In the early 1940s, the Eastman high-speed camera was able to take 1000 frames per second (fps) on 16 mm film [3]. Later, a 10 000 fps rotating prism camera was demonstrated [4]. In particular, high-speed imaging was revolutionized by electronic sensors based on the charge-coupled device (CCD) or complementary metal oxide semiconductor (CMOS), which enabled acquisition rates of up to $10^7$ fps [5]. However, due to the limitations of on-chip storage and electronic read-out speed, further increasing the frame rate is challenging, severely restricting the applications of CCD- or CMOS-based imaging technologies in measuring faster dynamic scenes [6].

Recently, several ultrafast imaging techniques have been developed, such as sequentially timed all-optical mapping photography (STAMP) [7], compressed ultrafast spectral-temporal (CUST) photography [8], compressed ultrafast photography (CUP) [9–15], and serial time-encoded amplified imaging (STEAM) [16,17]. STAMP and CUST utilize a chirped laser pulse for illumination and transform the spectral components into temporal information. Therefore, these two techniques operate on an active imaging mode, which rules out the imaging of a luminescent object. CUP is a passive ultrafast imaging technique, which combines streak imaging and compressed sensing. However, CUP employs a streak camera as an imaging device [9,18],

*sazhang@phy.ecnu.edu.cn
†shxxu@szu.edu.cn
‡zrsun@phy.ecnu.edu.cn

 

which limits practical applications due to the high cost of the streak camera. STEAM demands special active illumination, and it has a low temporal resolution of about 100 ns.

The electro-optical deflector can vary the input-light propagation direction within a certain angle at a high speed [19–22], and therefore, it is successfully used in ultrafast imaging, such as the crystal streak camera [23,24]. In this imaging application, the electro-optical deflector transforms the temporal information into a spatial distribution. However, only the dynamic information of a one-dimensional (1D) image can be recorded because of the small deflection angle (a few milliradians). Usually, to record dynamic information of a two-dimensional (2D) image in deflection imaging, the image-size distance on the CCD or CMOS detector is necessary to distinguish two adjacent frames, similar to a rotating framing camera [25]. Obviously, the small deflection angle of the electro-optical deflector will result in spatiotemporal mixing along the deflection direction, when the dynamic information of the 2D image is recorded.

To overcome the limitation of the electro-optical deflector in 2D ultrafast imaging, here, we develop the ultrafast electro-optical deflector imaging (UEODI) technique. In our method, all of the 2D images are encoded in the dynamic scene, each encoded image is deflected by the electro-optical deflector; all of the encoded and deflected images are superposed; and, finally, the original images are recovered using an augmented Lagrangian (AL) algorithm, which belongs to the compressed sensing technique [26–28]. In our scheme, the pixel-size distance on the CCD or CMOS detector can distinguish the two adjacent images, instead of the image-size distance, and thus, greatly improves the temporal resolution. In our UEODI system, the temporal resolution is approximately 20 ps, corresponding to a frame rate of $5 \times 10^{10}$ fps, which is mainly limited by the deflection velocity of the electro-optical deflector, and the dynamic spatial resolutions along the vertical and horizontal directions are 0.89 and 0.79 line pairs per mm (lp/mm), respectively, with a field of view (FOV) of $25 \times 25$ mm$^2$. Moreover, UEODI can detect a three-dimensional (3D) object when combined with the time-of-flight (TOF) method. In addition, UEODI is a single-shot receive-only imaging method, which is highly advantageous for imaging nonrepetitive transient events or fast luminescent processes. To demonstrate the ability of 2D ultrafast imaging and 3D object detection via UEODI, we successfully visualize a molecular photoluminescent process and measure a 3D ladder structure.

## II. BASIC PRINCIPLE

A schematic diagram of the data acquisition and reconstruction in UEODI is shown in Fig. 1. For the data acquisition, the 3D datacube $X$ (i.e., the dynamic scene) is first encoded spatially by random codes, then deflected temporally by the electro-optical deflector, and finally integrated spatiotemporally on the detector array to form the 2D data $Y$, as shown in Fig. 1(a). Mathematically, this process is equivalent to successively applying a spatial encoding operator $\mathbf{E}$, a temporal deflecting operator, $\mathbf{D}$, and a spatiotemporal integration operator, $\mathbf{I}$, to the intensity distribution of the input dynamic scene, $X$, as expressed by

$$Y = \mathbf{IDE}X. \tag{1}$$

$\mathbf{L}$ is used to represent the combined linear operator, that is, $\mathbf{L} = \mathbf{IDE}$. Then, Eq. (1) can be written as

$$Y = \mathbf{L}X. \tag{2}$$

To reconstruct the input dynamic scene $X$, the inverse problem of Eq. (2) must be solved. Given the operator $\mathbf{L}$, we can reasonably estimate the dynamic scene $X$ from measurement $Y$ by adopting the AL algorithm [26–28], belonging to the compressed sensing technique. Image reconstruction using the AL algorithm can be mathematically formulated as

$$\min_X L(X) = \Phi(X) - \lambda(Y - \mathbf{L}X) + \frac{\beta}{2}||Y - \mathbf{L}X||_2^2, \tag{3}$$

where $\lambda$ is a Lagrange multiplier and $\beta$ is the penalty parameter. $Y$–$\mathbf{L}X$ represents the measurement fidelity and $\|\cdot\|_2$ denotes the $l_2$ norm. In addition, $\Phi(X)$ denotes the total variation (TV) norm and is often used as the regularizer in image restoration [26,29]; it is given by

$$\Phi(X) = ||\mathbf{D}X||_2 \tag{4}$$

where $\mathbf{D}$ is the gradient operator, which means that $\mathbf{D}X$ is the gradient of $X$.

In our scheme, as shown in Fig. 1(a), the dynamic scene is randomly encoded in the space. Because of the temporal deflecting operation in the imaging process, these random codes in each moment of the dynamic scene are irrelevant. Thus, the image in each moment can be recovered based on its own codes. Consequently, the original dynamic scene can be reconstructed by using these random codes. In our image reconstruction, as shown in Fig. 1(b), we set all of the initial elements of $X^0$ in the 3D datacube to zero. In each iteration step, datacube $X^i$ ($i$ represents the $i$th iteration) is recalculated by utilizing the measurement image $Y$ and the random codes $\mathbf{C}$ based on an alternating minimization algorithm [26–28]. In this process, $L(X)^i$ is separately minimized by a shrinkagelike formula when $\mathbf{D}X^i$ is considered as a variable, while it is minimized by a one-step steepest descent scheme when $X^i$ is regarded as a variable. Thus, $X^{i+1}$ is obtained by this alternating minimization process. When the difference between the two

object functions, $L(X)^i$ and $L(X)^{i+1}$, is smaller than the threshold value, the object function, $L(X)$, is considered to be convergent and the images are correctly reconstructed.

To show the 2D ultrafast imaging based on image encoding and decoding, we theoretically simulate the dynamic scene with two orientation phantoms appearing alternatingly, and the simulation results are shown in the inset of Fig. 1(b), wherein the upper panel shows the original images, and the lower panel shows the reconstructed results. Clearly, the reconstructed images are consistent with the original ones, and thus, demonstrate the feasibility of UEODI. In the image reconstruction, there are some restrictions. Generally, these restrictions are relative to the data compressed ratio from three-dimensional scene to two-dimensional image and the sparsity of the dynamic scene. If the dynamic scene has low sparsity and the data acquisition needs a high compression ratio, the reconstructed images will be blurred for some details, including the spatial structure and temporal evolution. However, if the dynamic scene has low sparsity and the data acquisition needs a low compression ratio, the reconstructed images can usually retain the true details, such as the reconstructed images in the inset of Fig. 1(b). A similar situation can be found for the dynamic scene with high sparsity and data acquisition with a high compression ratio. In a real experiment, the dynamic scene often has a simple texture, and thus, it has high sparsity. Therefore, data acquisition allows a high compression ratio.

## III. EXPERIMENTAL SETUP

The experimental configuration of UEODI is shown in Fig. 2. First, the dynamic scene or object is imaged on a DMD using a camera lens. Here, a Glan polarizer is placed behind the camera lens to generate linearly polarized light or to change the light polarization direction. To encode the dynamic scene, a pseudorandom binary pattern is generated on the DMD via a personal computer.

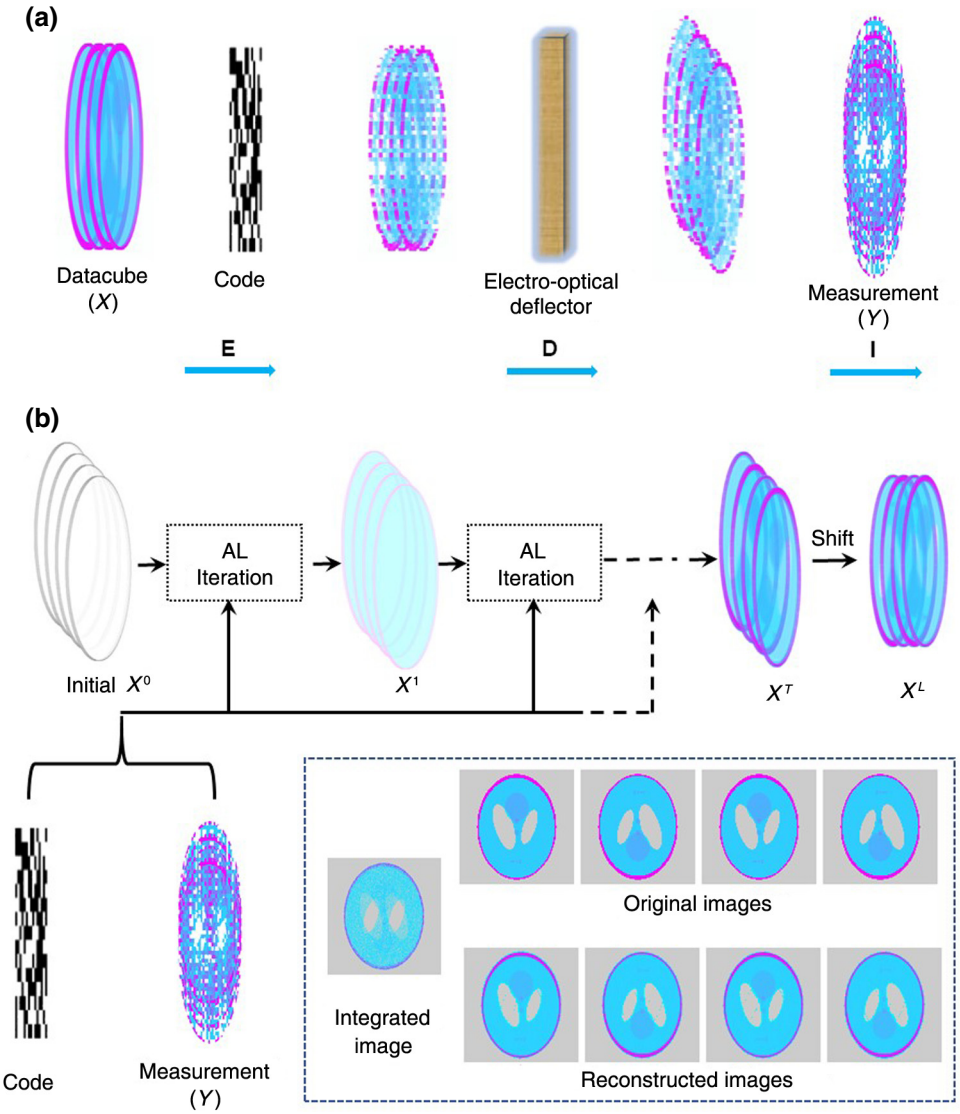


FIG. 1. Data acquisition and image reconstruction. (a) Data acquisition, $X$: original datacube; $Y$: measurement result; **E**: spatial encoding operator; **D**: temporal deflecting operator; and **I**: spatiotemporal integration operator. (b) Data reconstruction and simulation results for the rotated phantom (inset pictures). Here, the dashed arrows indicate the middle iteration processes.

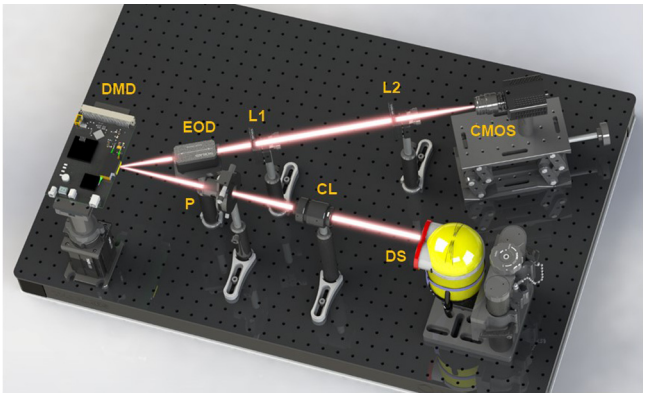


FIG. 2. UEODI system configuration. CMOS (Andor ZYLA4.2 PLUS); EOD, electro-optical deflector; DMD, digital micromirror device (Texas Instruments, DLP LightCrafter); P, Glan polarizer (Newport, RM25A); CL, camera lens; DS, dynamic scene; L1 and L2, lenses.

Then, the encoded dynamical scene reflected from DMD is deflected by an electro-optical deflector that is composed of an electro-optical crystal (41K-BB, Quantum Technology, Inc.) with a deflection efficiency of 2.5 mrad/kV and a custom-made ultrafast high-voltage power source (Minyang Device, Inc.) with a time response within 700 ps. Finally, the deflected dynamic scene is measured by a CMOS camera through a 4f imaging system with two tube lenses with 100 and 300 mm focal lengths. The CMOS camera has $2048 \times 2048$ pixels, but only $1000 \times 1060$ pixels are utilized in our UEODI system. In the experiment, each image involves $1000 \times 1000$ pixels, and the dynamic scene can be maximally deflected by 60 pixels in the vertical direction by applying the highest voltage on the electro-optical crystal. Thus, a $1000 \times 1000 \times 60$ datacube can be recorded in our UEODI system with a single-shot measurement. That is, 60 frames of images can be reconstructed in our experiment.

## IV. RESULTS AND DISCUSSION

The temporal resolution is a very important parameter for characterizing the system performance of UEODI. Here, we transform the spatial distance into temporal information by utilizing the TOF method, that is, the time difference is characterized by the spatial distance with $\Delta t = 2\Delta L/c$, where $c$ is the velocity of light and $\Delta L$ is the distance between the two measured objects. The experimental arrangement is shown in Fig. 3(a). A Ti-sapphire laser amplifier (Spectra-physics, Spitfire ACE) is used to generate the femtosecond laser with a pulse width of 50 fs, a central wavelength of 800 nm, and a repetition rate of 10 Hz. The output pulse laser is diffused by a concave lens diffuser, and it irradiates two plastic stakes (labeled "1" and "2"), where the distance of the two plastic stakes can be adjusted. The width of the plastic stake is 3 mm and its length is 15 mm. The UEODI device collects backscattered photons from the stake surfaces. In the experiment, we fix the distances of the two plastic stakes at 1.5, 3, and 4.5 mm, corresponding to time intervals of 10, 20, and 30 ps, respectively. Figures 3(b)–3(d) show the reconstructed images obtained using the three time intervals, wherein the left panel shows the reconstructed close "1" plastic stake and the right panel shows the reconstructed far "2" plastic stake. For a time interval of 10 ps, the two plastic stakes simultaneously appear and their intensities are almost indistinguishable. This phenomenon is similar to that of a slow-speed camera that cannot distinguish fast-moving events. When the time interval is increased to 20 or 30 ps, the two plastic stakes appear sequentially and the difference in their intensities can be clearly observed. Based on experimental observations, we can conclude that the temporal resolution of our UEODI device is approximately 20 ps, corresponding to an imaging speed of $5 \times 10^{10}$ fps.

Although spatial resolution can be adjusted by tuning the numerical aperture (NA) of the camera lens, the spatial resolution of UEODI under our experimental conditions must be characterized. Here, we image one part of the 1951 USAF resolution test chart, illuminated by two diffused laser pulses, and the experimental design is shown in Fig. 4(a). Here, the two pulses have a slight difference in intensity and are separated by a 3 ns delay in time order. We measure the static scene without electro-optical deflection, and the experimental result is shown in Fig. 4(b), wherein the FOV is approximately $25 \times 25$ mm$^2$, and only elements 3, 4, 5, and 6 in group –1 are recorded. The reconstructed dynamic images with electro-optical deflection are shown in Fig. 4(c). Compared with that of the static image, the quality of the dynamic images is relatively poor because the dynamic images are obtained by encoding, superposition, and reconstruction. Moreover, the vertical lines are clearer than the horizontal ones. The basic reason for this difference in clarity is that the dynamic scene is deflected along the vertical direction by the electro-optical crystal. To intuitively show the spatial resolution, the two lines of each element in the left reconstructed image of Fig. 4(c) are integrated along the horizontal and vertical directions, and the calculated results are shown in Fig. 4(d). In element 6, the vertical lines can be distinguished, but the horizontal lines cannot. However, both the horizontal and vertical lines can be distinguished in elements from 3 to 5. UEODI cannot distinguish the narrower lines, such as element 1 in group 0, even for the vertical lines. In element 5, the width of the line is approximately 629 $\mu$m, and the dynamic spatial resolution is calculated to be 0.79 lp/mm. In element 6, the width of the lines is approximately 561 $\mu$m, and the spatial resolution is determined to be 0.89 lp/mm. Thus, the dynamic spatial resolutions of UEODI along the vertical and horizontal directions are determined to be 0.79 and 0.89 lp/mm, respectively. To

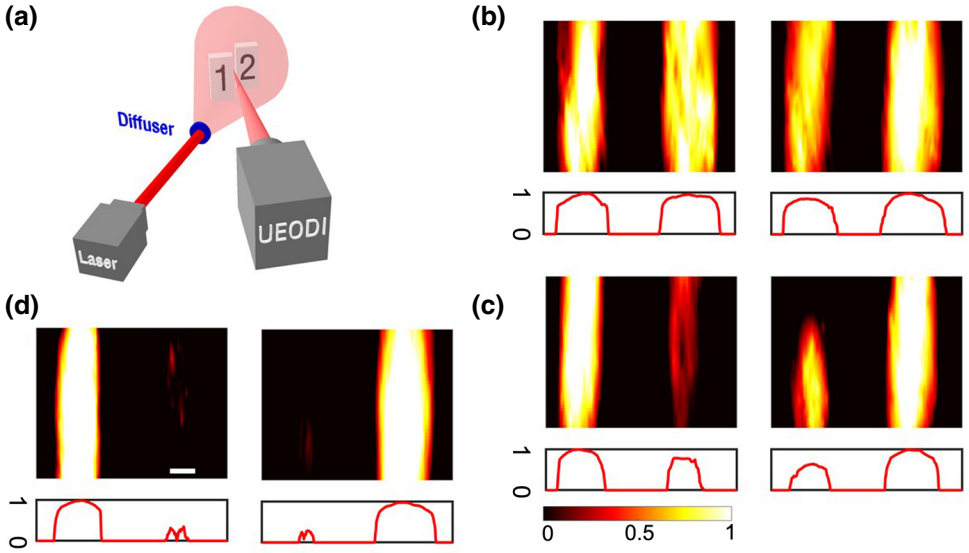


FIG. 3. Characterizing temporal resolution. (a) Experimental setup, wherein the distance between two plastic stakes ("1" and "2") can be precisely adjusted. (b)–(d) Reconstructed images with time intervals between the two plastic stakes of 10, 20, and 30 ps, respectively. Scale bar: 1 mm.

demonstrate the information capacity of an image, we calculate the space-bandwidth product (SBP) [30], which can be obtained by the relationship of $N_{\mathrm{SBP}} = (L_v/B_v)\,(L_r/B_r)$, where $L_v$ and $L_r$ are the length and width in the FOV, respectively, and $B_v$ and $B_r$ are the widths of the horizontal and vertical lines, respectively. Based on the FOV size ($25 \times 25$ mm$^2$) and the line widths (0.629 and 0.561 mm) in our experiment, the $N_{\mathrm{SBP}}$ value is calculated to be 1771.

To show that UEODI can capture ultrafast dynamic events, we measure a photoluminescent process with Rhodamine B, and the experimental arrangement is shown in Fig. 5(a). Rhodamine B dissolved in absolute ethyl alcohol is excited by a femtosecond laser with a pulse width of 50 fs and a central wavelength of 800 nm, and UEODI measures the fluorescent signal in the perpendicular direction of the laser propagation. Figure 5(b) shows the image reconstruction results obtained for the time interval of 500 ps. The whole evolution process of the fluorescence signal from appearance to disappearance can be clearly observed. To directly display the photoluminescent process, we calculate the total intensity by summing all of the pixel values in each image, and the calculated results are shown in Fig. 5(c) (red squares). In the fluorescent decay component, we use an exponential function, $e^{(-t/\tau)}$, for the fitting (blue line), where $\tau$ is the lifetime. We obtain a value of $\tau$ of 2.84 ns, which is close to that in a previous report [31]. In addition, we use the streak camera to measure the dynamic evolution of the fluorescence signal, and the measured result is also shown in Fig. 5(c) (cyan circles). A comparison of the photoluminescent processes

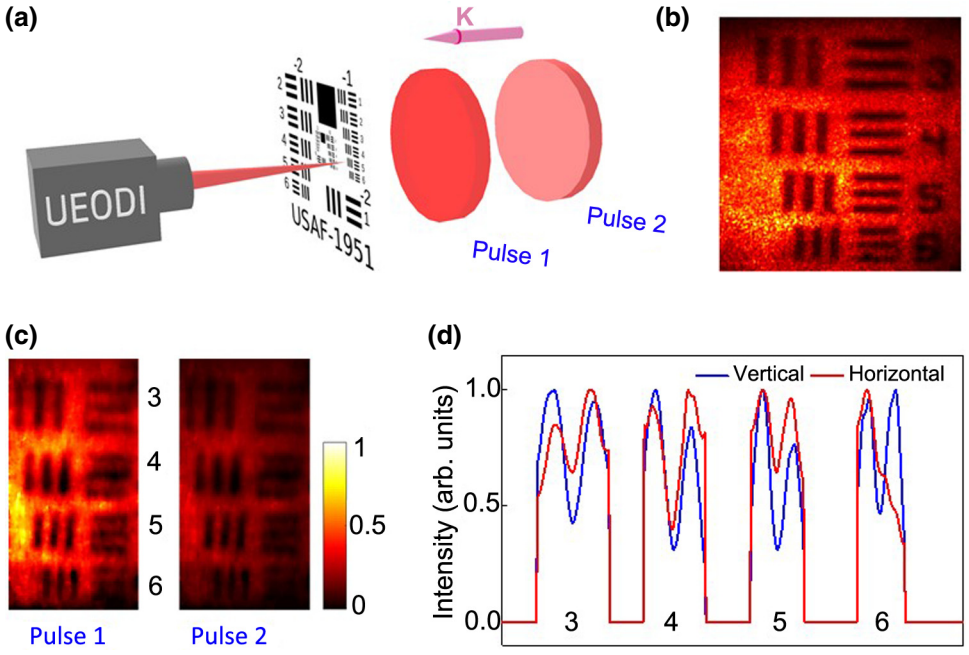


FIG. 4. Characterizing dynamic spatial resolution. (a) Experimental setup for two delayed laser pulses irradiating a 1951 USAF resolution test chart, where **K** is the wave vector. (b) Static image for elements 3, 4, 5, and 6 in group –1 of the 1951 USAF resolution test chart. (c) Reconstructed dynamic images. (d) Integrated intensity along the horizontal or vertical axis for each element.

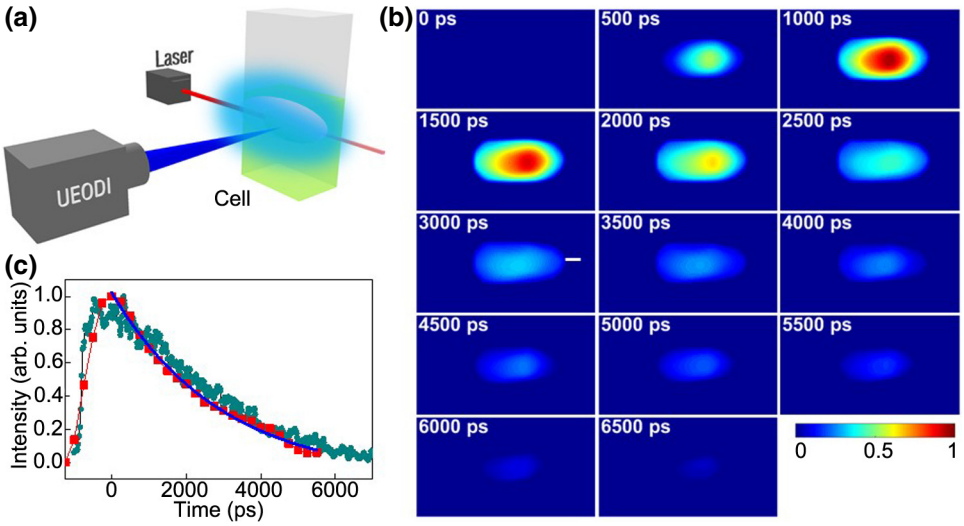


FIG. 5. Recording a molecular photoluminescent process. (a) Experimental design. (b) Reconstructed images of the luminescent process. (c) Calculated fluorescence intensity evolution (red squares), together with the exponential fitting (blue line) and the measured result obtained by the streak camera for comparison (cyan circles). Scale bar: 3 mm.

measured by the two methods shows that the obtained results are almost identical, but UEODI can also provide spatial information at each moment.

The 3D imaging technique is widely employed in many application areas, such as biology, remote sensing. and entertainment [32–34]. The most common approach for 3D imaging is based on TOF detection [35–39]. In combination with the TOF technique, UEODI can also directly map a 3D object. To show that the combined approach can detect a 3D object, we map a ladder structure, and the experimental arrangement is shown in Fig. 6(a). In the experiment, the ladder has four steps, and the height, width, and length of each step are 7.5, 3, and 25 mm, respectively. The height of 7.5 mm corresponds to a time of

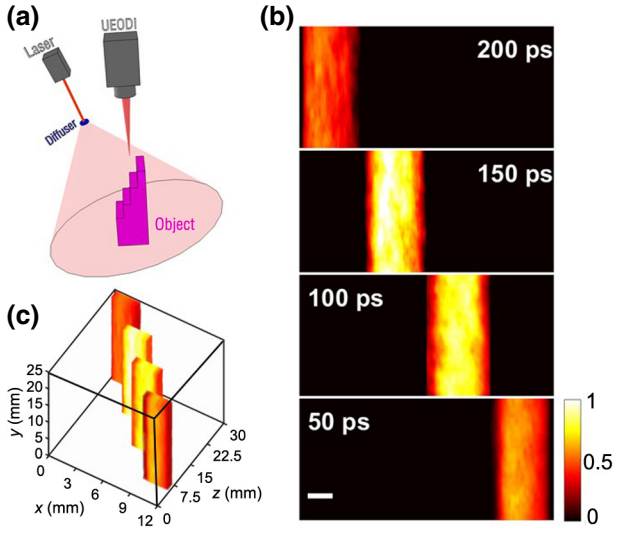


FIG. 6. Mapping a 3D ladder structure. (a) Experimental design, wherein the height of each step is 7.5 mm, the width is 3 mm, and the length is 25 mm. (b) Reconstructed images at times of 50, 100, 150, and 200 ps. (c) Recovered 3D ladder structure. Scale bar: 2 mm.

50 ps, which is larger than the temporal resolution (20 ps) of our UEODI system. First, the diffused laser illuminates the ladder. Then, UEODI collects backscattered photons from the surface of the ladder. Finally, the AL algorithm recovers the ladder structure. The reconstructed images at each moment are shown in Fig. 6(b). Clearly, each step can be individually distinguished. The spatial depth ($z$) can be calculated according to the temporal information ($t$) and is given by $z = ct/2$. Based on the reconstructed images in Fig. 6(b), we recover the ladder structure, as shown in Fig. 6(c). The recovered ladder structure is in good agreement with the real object shape. In our UEODI system, the temporal resolution is approximately 20 ps, and the depth resolution for the 3D object detection is 3 mm. Therefore, our device enables mapping of a 3D object with a longitudinal resolution of 3 mm and lateral resolutions of 629 (vertical) and 561 $\mu$m (horizontal), respectively.

CUP is another 2D ultrafast imaging technique [9–15]. The main difference between UEODI and CUP is the imaging deflection method. UEODI utilizes the electro-optical crystal in combination with a CMOS camera, while the CUP employs the streak camera. The electro-optical crystal deflects the photons by the Pockels effect, while the streak camera deflects the electrons by the electric field. Both deflection methods can achieve a very high temporal resolution in the femtosecond region. However, the streak camera is usually applied in 1D ultrafast imaging and has great limitations for 2D ultrafast imaging. In the streak camera [18], the photons are transformed into the electrons, then the electrons are deflected in the steak tube, and finally the electrons are converted into the photons again. If the electron density in the transient event is high, the electrons will diffuse due to the Coulomb repulsive force [40,41]. Thus, the measured image will be blurred and the spatial resolution is greatly reduced. Moreover, the streak camera is very expensive, which greatly limits practical applications. On the contrary, the electro-optical

crystal is cheap and it just operates the photons, which is beneficial for keeping the original image shape. These advantages can promote the marketization and applications of UEODI. Additionally, the UEODI adopts an AL algorithm. Compared with the TwIST (Two-Step Iterative Shrinkage/Thresholding) algorithm in the CUP, the AL algorithm has advantages in the quality and stability of the image reconstruction [15,26–28]. The temporal resolution of UEODI in our system is 20 ps, which is close to that of picosecond CUP, while lower than that of femtosecond CUP in previous works [9–15], but UEODI also has the ability to obtain similar temporal resolution by optimizing the optical system. The time response of the electro-optical crystal via the Pockels effect is very fast, which can be in the femtosecond region, and thus, the temporal resolution of UEODI is mainly limited by the power source. In the future, we can use a power source with a faster time response to increase the temporal resolution. An alternative way to increase the temporal resolution is to employ an optical-deflection accelerating technique [42,43], which can amplify the deflection angle by one to two orders of magnitude by adjusting the curvature of the curved surface. Therefore, by applying both the power source with a faster time response and the optical-deflection accelerating device, the temporal resolution of UEODI is expected to be upgraded to a new level.

## V. CONCLUSIONS

We develop a 2D ultrafast imaging technique, namely, UEODI. This UEODI technique is based on 3D image reconstruction that combines electro-optical deflection imaging with the AL algorithm, opening up an alternative route for ultrafast optical imaging. In our UEODI system, the temporal resolution of UEODI is 20 ps, and the dynamic spatial resolutions along the vertical and horizontal directions are 0.89 and 0.79 lp/mm, respectively, with a $25 \times 25$ mm$^2$ FOV. When combined with the TOF method, our UEODI system can map a 3D object with a longitudinal resolution of 3 mm and lateral resolutions of 561 (vertical) and 629 $\mu$m (horizontal), respectively. Using UEODI, we successfully visualize a molecular luminescent process and map a 3D ladder structure. Moreover, UEODI can be coupled to a variety of imaging modalities and provides more powerful temporal and spatial imaging. Given the advantages of UEODI related to the single-shot receive-only nature and higher temporal and dynamic spatial resolutions, we expect that UEODI will have widespread applications in physics, chemistry, biology, and even information science.

## ACKNOWLEDGMENTS

This work is partially supported by the National Natural Science Foundation of China (Grants No. 91850202, No. 11727810, No. 11774094, No. 61720106009, No. 61775142, and No. 61571271), the Science and Technology Commission of Shanghai Municipality (Grants No. 17ZR146900 and No. 16520721200), the Program of Introducing Talents of Discipline to Universities 111 project (Grant No. B12024), the China Postdoctoral Science Foundation (Grant No. 2018M641958), and the Shenzhen basic research project on subject layout (Grant No. JCYJ20170412105812811).

[1] E. Muybridge, The science of the horse's motions, Sci. Am. **39**, 241 (1878).
[2] E. Mach and P. Salcher, Photographische Fixirung der durch Projectile in der Luft eingeleiteten Vorgänge, Ann. Phys. **268**, 277 (1887).
[3] J. Boon, The eastman high-speed camera, type iii, J. Soc. Motion Pict. Eng. **43**, 321 (1944).
[4] J. H. Waddell, The rotating-prism camera: An historical survey, J. SMPTE **75**, 666 (1966).
[5] Y. Kondo, K. Takubo, H. Tominaga, R. Hirose, N. Tokuoka, Y. Kawaguch, Y. Takaie, A. Ozaki, S. Nakaya, F. Yano, and T. Daigen, Development of "HyperVision HPV-X" high-speed video camera, Shimadzu Rev. **69**, 285 (2012).
[6] M. El-Desouki, M. J. Deen, Q. Fang, L. Liu, F. Tse, and D. Armstrong, CMOS image sensors for high speed applications, Sensors **9**, 430 (2009).
[7] K. Nakagawa, A. Lwasaki, Y. Oishi, R. Horisaki, A. Tsukamoto, A. Nakamura, K. Hirosawa, H. Liao, T. Ushida, K. Goda, K. Kannari, and I. Sakuma, Sequentially timed all-optical mapping photography (STAMP), Nat. Photonics **8**, 695 (2014).
[8] Y. Lu, T. T. Wong, F. Chen, and L. Wang, Compressed Ultrafast Spectral-Temporal Photography, Phys. Rev. Lett. **122**, 193904 (2019).
[9] L. Gao, J. Liang, C. Li, and L. V. Wang, Single-shot compressed ultrafast photography at one hundred billion frames per second, Nature **516**, 74 (2014).
[10] J. Liang, C. Ma, L. Zhu, Y. Chen, L. Gao, and L. V. Wang, Single-shot real-time video recording of a photonic Mach cone induced by a scattered light pulse, Sci. Adv. **3**, e1601814 (2017).
[11] L. Zhu, Y. Chen, J. Liang, Q. Xu, L. Gao, C. Ma, and L. V. Wang, Space- and intensity-constrained reconstruction for compressed ultrafast photography, Optica **3**, 694 (2016).
[12] C. Yang, D. Qi, X. Wang, F. Cao, Y. He, W. Wen, T. Jia, J. Tian, Z. Sun, L. Gao, S. Zhang, and L. V. Wang, Optimizing codes for compressed ultrafast photography by the genetic algorithm, Optica **5**, 147 (2018).
[13] J. Liang, L. Zhu, L. Zhu, and L. V. Wang, Single-shot real-time femtosecond imaging of temporal focusing, Light: Sci. Appl. **7**, 42 (2018).
[14] C. Yang, D. Qi, J. Liang, X. Wang, F. Cao, Y. He, X. Ouyang, B. Zhu, W. Wen, T. Jia, J. Tian, L. Gao, Z. Sun, S. Zhang, and L. V. Wang, Compressed ultrafast photography multi-encoding imaging, Laser Phys. Lett. **15**, 116202 (2018).
[15] C. Yang, D. Qi, F. Cao, Y. He, X. Wang, W. Wen, J. Tian, J. Tian, Z. Sun, and S. Zhang, Improving the image reconstruction quality of compressed ultrafast photography

via an augmented Lagrangian algorithm, J. Opt. **21**, 035703 (2019).
[16] K. Goda, K. K. Tsia, and B. Jalali, Serial time-encoded amplified imaging for real-time observation of fast dynamic phenomena, Nature **458**, 1145 (2009).
[17] J. L. Wu, Y. Q. Xu, J. J. Xu, X. M. Wei, A. C. Chan, A. H. Tang, K. L. Lau, B. M. Chung, H. C. Shum, E. Y. Lam, K. K. Yong, and K. K. Tsia, Ultrafast laser-scanning time-stretch imaging at visible wavelengths, Light: Sci. Appl. **6**, e16196 (2017).
[18] Hamamatsu, https://www.hamamatsu.com/jp/en/product/photometry-systems/streak-camera/index.html
[19] J. A. Valdmanis, G. Mourou, and W. Gabel, Picosecond electro-optic sampling system, Appl. Phys. Lett. **41**, 211 (1982).
[20] M. S. Woody, M. Capitanio, E. M. Ostap, and Y. E. Goldman, Electro-optic deflectors deliver advantages over acousto-optical deflectors in a high resolution, ultra-fast force-clamp optical trap, Opt. Express **26**, 11181 (2018).
[21] S. Ma, H. Yu, H. Zhang, X. Han, Q. Lu, C. Ma, R. I. Boughton, and J. Wang, Efficient high repetition rate electro-optic Q-switched laser with an optically active langasite crystal, Sci. Rep. **6**, 30517 (2016).
[22] Y. Chiu, D. D. Stancil, T. E. Schlesinger, and W. P. Risk, Electro-optic beam scanner in ktiopo4, Appl. Phys. Lett. **69**, 3134 (1996).
[23] C. L. M. Ireland, The use of a $LiNbO_3$ deflector in a $\backsim$100 ps resolution streak camera, Opt. Commun. **27**, 459 (1978).
[24] C. L. M. Ireland, A $\sim$20 ps resolution crystal streak camera, Opt. Commun. **30**, 99 (1979).
[25] H. Edels and D. Whittaker, The theory and design of rotating mirror cameras, J. Sci. Instrum. **32**, 103 (1955).
[26] M. V. Afonso, J. M. Bioucas-Dias, and M. A. Figueiredo, An augmented Lagrangian approach to the constrained optimization formulation of imaging inverse problems, IEEE Trans. Image Process. **20**, 681 (2011).
[27] C. Li, *An Efficient Algorithm for Total Variation Regularization with Applications to the Single Pixel Camera and Compressive Sensing* (Rice University, Houston, 2010).
[28] Y. Wang, J. Yang, W. Yin, and Y. Zhang, A new alternating minimization algorithm for total variation image reconstruction, SIAM J. Imaging Sci. **1**, 248 (2008).
[29] A. Chambolle, An algorithm for total variation minimization and applications, J. Math. Imaging Vision **20**, 89 (2004).
[30] A. W. Lohmann, R. G. Dorsch, D. Mendlovic, C. Ferreira, and Z. Zalevsky, Space–bandwidth product of optical signals and systems, J. Opt. Soc. Am. A **13**, 470 (1996).
[31] A. S. Kristoffersen, S. R. Erga, B. Hamre, and Ø Frette, Testing fluorescence lifetime standards using two-photon excitation and time-domain instrumentation: Rhodamine B, coumarin 6 and lucifer yellow, J. Fluoresc. **24**, 1015 (2014).
[32] K. Omasa, F. Hosoi, and A. Konishi, 3D lidar imaging for detecting and understanding plant responses and canopy structure, J. Exp. Bot. **58**, 881 (2007).
[33] S. L. Liu, J. Li, Z. L. Zhang, Z. G. Wang, Z. Q. Tian, G. P. Wang, and D. W. Pang, Fast and high-accuracy localization for three-dimensional single-particle tracking, Sci. Rep. **3**, 2462 (2013).
[34] B. Javidi, F. Okano, and J.-Y. Son, *Tree-Dimensional Imaging, Visualization, and Display* (Springer, New York, 2009).
[35] J. Sell and P. O'Connor, The xbox one system on a chip and kinect sensor, IEEE Micro **34**, 44 (2014).
[36] A. Mccarthy, N. J. Krichel, N. R. Gemmell, X. Ren, M. G. Tanner, S. N. Dorenbos, V. Zwillwer, R. H. Hadfield, and G. S. Buller, Kilometer-range, high resolution depth imaging via 1560 nm wavelength single-photon detection, Opt. Express **21**, 8904 (2013).
[37] Advanced Scientifc Concepts, Products overview, http://www.advancedscientifcconcepts.com/products/products.html Accessed at: 8/28/2018.
[38] R. D. Richmond, Eye-safe laser radar 3d imaging, Proc. SPIE **4377**, 23 (2001).
[39] J. Liang, L. Gao, P. Hai, C. Li, and L. V. Wang, Encrypted three-dimensional dynamic imaging using snapshot time-of-flight compressed ultrafast photography, Sci. Rep. **5**, 15504 (2015).
[40] R. Chatelain, *Radio-Frequency Pulse Compression for High-Brightness Ultrafast Electron Diffraction: Design, Characterization and Application* (McGill University, Montréal, 2014).
[41] F. O. Kirchner, S. Lahme, F. Krausz, and P. Baum, Coherence of femtosecond single electrons exceeds biomolecular dimensions, New J. Phys. **15**, 063021 (2013).
[42] Y. Ai, H. Chen, J. Li, Q. Wu, and Y. Cai, Optical-deflection accelerating techniques in streak camera, J. Shenzhen Univ. Sci. Eng. **33**, 134 (2016).
[43] Y. Ai and J. Li, *in Photonics and Optoelectronics* (IEEE, 2012), pp. 1–3.